



HAL
open science

Pressure-driven micro-poro-mechanics: A variational framework for modeling the response of porous materials

Felipe Álvarez-Barrientos, Daniel E Hurtado, Martin Genet

► To cite this version:

Felipe Álvarez-Barrientos, Daniel E Hurtado, Martin Genet. Pressure-driven micro-poro-mechanics: A variational framework for modeling the response of porous materials. *International Journal of Engineering Science*, 2021, 169, pp.103586. 10.1016/j.ijengsci.2021.103586 . hal-03364755

HAL Id: hal-03364755

<https://hal.science/hal-03364755>

Submitted on 5 Oct 2021

HAL is a multi-disciplinary open access archive for the deposit and dissemination of scientific research documents, whether they are published or not. The documents may come from teaching and research institutions in France or abroad, or from public or private research centers.

L'archive ouverte pluridisciplinaire **HAL**, est destinée au dépôt et à la diffusion de documents scientifiques de niveau recherche, publiés ou non, émanant des établissements d'enseignement et de recherche français ou étrangers, des laboratoires publics ou privés.

Pressure-driven micro-poro-mechanics: A variational framework for modeling the response of porous materials

Felipe Álvarez-Barrientos^a, Daniel E. Hurtado^{a,b,1}, Martin Genet^{c,d}

^a*Department of Structural and Geotechnical Engineering, School of Engineering, Pontificia Universidad Católica de Chile, Santiago, Chile, Vicuña Mackenna 4860, Santiago, Chile*

^b*Institute for Biological and Medical Engineering, Schools of Engineering, Medicine and Biological Sciences, Pontificia Universidad Católica de Chile, Vicuña Mackenna 4860, Santiago, Chile*

^c*Laboratoire de Mécanique des Solides (LMS), École Polytechnique/CNRS/Institut Polytechnique de Paris, Palaiseau, France*

^d*Inria, Palaiseau, France*

Abstract

Porous materials are highly relevant in engineering and medical applications due to their enhanced properties and lightweight nature. Current micromechanical models of porous materials can accurately predict the response under the assumptions of small deformations and drained conditions, typically driven by imposed deformations. However, the theoretical framework for the micromechanical modeling of porous material driven by pore pressure in the large-deformation range has been understudied. In this work, we develop a finite-deformation variational framework for pressure-driven foams, i.e., materials where the pore pressure in the cavities produces the deformation. We further consider different kinematical constraints in the formulation of boundary conditions: kinematic uniform displacements, periodic displacements and uniform traction. We apply the proposed model in the numerical simulation of lung porous tissue using a spherical alveolar geometry and an image-based geometry obtained from micro-computed-tomography images of rat lung. Our results show that the stress distributions in the spherical alveolar model are highly dependent on the kinematical constraints. In contrast, the stress distribution in the image-based alveolar model is not affected by the choice of boundary conditions. Further, when comparing the response of pressure-driven versus deformation-driven models, we conclude that hydrostatic stresses experience a marked shift in their distribution, whereas the deviatoric stresses remain unaffected. Our findings of how stresses are affected by the choice of boundary conditions and geometry take particular relevance in the simulation of the lungs, where the pressure-driven and deformation-driven cases are related to mechanical ventilation and spontaneous breathing.

Keywords: Open-cell Foam Material, Micromechanics of Porous Materials, Lung Mechanics, Poromechanics, Pressure-driven Models

*Corresponding Author: Daniel E. Hurtado, email address: dhurtado@ing.puc.cl, Phone: +562 2354 4207

1. Introduction

Porous materials are ubiquitous in nature and engineering applications, and take shape as saturated rocks, polymer foams, plant cells and biological tissues among others. One kind of porous materials are open-cell foams (OCFs), which are defined as materials composed of a matrix with interconnected cavities (Ma et al., 2011). This structural arrangement strongly influences the mechanical response of OCFs, which is dominated by mechanisms such as bending of struts, buckling of cell walls, the formation of yield joints or folds, and fracture of cell struts and cell walls (Altenbach & Öchsner, 2010). Due to its permeability, cavities in OCFs can be subject to pressure exerted by a fluid or a gas, which can drive the mechanical response of the material. Examples of pressurized materials are the foams used to thermally insulate the Space Shuttle external tank (Bednarczyk et al., 2008), where thermoelastic and thermoinelastic effects are also present; the lung parenchyma, where alveoli are subject to internal air pressure (Koshiyama et al., 2019; Rausch et al., 2011; Sarabia-Vallejos et al., 2019); the brain tissue permeated by blood and cerebrospinal fluid (Guo et al., 2020); and porous elastomers, where the presence of pressurized cavities has proven to affect the overall response, producing, for instance, the shrinkage of elastomeric foams after demolding (Fen-Chong et al., 1999; Idiart & Lopez-Pamies, 2012).

The constitutive response of porous materials has been approached in engineering by means of traditional poromechanics theory, which focuses on a macroscopic approach (Biot, 1941; Chapelle & Moireau, 2014; Coussy, 2004), by use of the theory of porous media (Ehlers & Bluhm, 2002), which combines the theory of mixtures (Bowen, 1980, 1982; De Boer, 2000) with the concept of volume fractions, and also by explicitly considering fluid-structure interaction at the microscopic scale (Concha & Hurtado, 2020; Dormieux et al., 2002). Computational micromechanical models have been developed for many types of materials, but only few for OCFs, especially in the finite deformation setting. To this end, a representative volume element (RVE) of the underlying microstructure of the material must be constructed, based on which a microstructural problem is solved to obtain the stress and strain distributions in the RVE. Then, the effective behavior can be obtained by averaging the stress and strain fields arising in the RVE (Hashin, 1983; Hill, 1963; Suquet, 1987). In order to model OCFs, RVEs can be constructed from micro-computed-tomography (micro-CT) images of the microstructure, conferring the RVE a highly realistic geometry of the material, that allows to study the material response at the micro level. This approach has been used, for example, in models of polyurethane foams (Youssef et al., 2005), metallic foams (Kantzos et al., 2018) and pulmonary alveoli (Roth et al., 2017), giving information about local deformation mechanisms, such as regions of stress concentrations.

In addition to the creation of the RVE, micromechanical models of porous materials necessitate the definition of suitable boundary conditions (BCs), and internal loads. When experimental data is available, the boundary conditions in the RVE can be obtained from sets of 3D images using Digital Volume Correlation, or with methods to relate the conditions of the whole specimen to the conditions in the RVE, based on macroscopic homogenized

properties (Shakoor et al., 2017). However, in the lack of experimental data, and to avoid obtaining homogenized quantities, further assumptions have to be made to determine the boundary conditions of the RVE. One option is to use the classical boundary conditions adopted in homogenization and multi-scale simulations (Fish, 2013; Hill, 1963; Hollister & Kikuchi, 1992; Saeb et al., 2016; Suquet, 1987), where the displacement field is decomposed into an affine component and a fluctuation field, and according to the boundary condition selected, different constraints are applied in the fluctuation term. Five conditions are commonly adopted: i) Voigt bound model, where the displacement field is assumed to be affine everywhere inside the RVE and the fluctuation field vanishes, ii) kinematic uniform boundary condition (KUBC), where the fluctuation vanishes at the boundary but is otherwise unknown in the domain of the RVE, iii) periodic displacement boundary condition (PBC), where the fluctuation field is periodic at the boundary, iv) uniform traction boundary condition (SUBC), which can be interpreted as an integral constraint on the fluctuation field, and v) Reuss model, where the stress field is homogeneous everywhere inside the RVE. While the effect of these constraints on the coarse-scale response of composites is known (Carniel et al., 2019; Kanit et al., 2003; Terada et al., 2000), their implications on the microscopic stress fields in foams driven by pore pressure is still understudied. Such knowledge is fundamental in material modeling, as material phenomena such as plasticity and fracture initiate at microscopic scales driven by stresses that take place at the microstructure (Johnson & Cook, 1985).

Micromechanical analysis of foams have been focused on the cases where the macroscopic strain, or the macroscopic stress, are imposed (De Souza Neto & Feijóo, 2006; Perić et al., 2011). However, in porous materials the pore pressure can drive deformation, with the macroscopic strain and stress being a response of the system. For example, this case is present when the loading process of pressurized foams is decomposed into two steps: first, an initial configuration is obtained, where the deformation in the RVE is produced only by the pore pressure, and then, the final deformed configuration is obtained by applying the external loads. The pressure-driven case has been predominantly approached by means of numerical simulations, with less developments from an analytical perspective. To implement it, computational simulations have been conducted imposing restrictions between the degrees of freedom of the boundaries on the discretized system. Ma et al. (2011) developed a micromechanical model for fluid-filled closed-cell composites with pore pressure and external loads, where first they obtained the response with pore pressure only, imposing periodic boundary conditions by coupling constraint equations and obtaining the macroscopic strain as a result of the simulation. In another example, Ju et al. (2008) modeled balloon-expandable stents as cylindrical structures with longitudinal and circumferential periodicity, subject to internal pressure. Similar to the previous case, the elongation in the z -direction is unknown before finite element computations, and it is excluded from the displacement constraint equations by the use of multiple-point constraints. Despite the existence of these numerical constraints, which allow the pressure-driven model to be numerically solved, a general analysis of the boundary conditions for the continuous mechanical problem of pressurized foams remains an open avenue of research.

In this paper, we present a variational framework for modeling the pressure-driven response of RVEs of foam materials, in the setting of finite kinematics. The theoretical analysis of the problem is completed with the choice of boundary conditions, which are expressed as kinematical constraints in the fluctuation term of the displacement, among which three options are compared: KUBC, PBC and SUBC. After the variational framework is developed, the proposed model is used to study the micromechanical response in the context of lung parenchyma simulations. Moreover, the numerical simulations will help to understand the potential differences when the tissue microstructure is replaced by an idealized representation. We conclude by analyzing the implications of the different boundary conditions (KUBC, PBC and SUBC), and loadings (pressure, deformation), in terms of the stress distributions obtained.

2. Micromechanical Model: Variational Framework

In the following, we develop a variational framework for finite-strain micromechanical analysis of pressure-driven foam materials, i.e., porous materials for which the pore pressure is known and the macroscopic strain is an unknown of the problem. Let Ω_0^S and Ω^S be the solid domain in the reference and current configurations, respectively, and let Ω_0^F and Ω^F represent the fluid domain in the reference and current configurations, respectively. Then, the RVE domain in the reference configuration is $\Omega_0 = \Omega_0^S \cup \Omega_0^F$. Similarly, the current configuration is constructed as $\Omega = \Omega^S \cup \Omega^F$. Let $\partial\Omega_0^E$ and $\partial\Omega_0^N$ be the outer and inner boundaries, respectively, in the reference configuration, and $\partial\Omega^E$ and $\partial\Omega^N$ be their counterparts in the current configuration, see Figure 1a for a graphical representation. Note that, in general, $\partial\Omega_0^E$ is only a subset of the total boundary of the RVE, because in OCFs the pores intersect the RVE border. The deformation mapping $\varphi : \Omega_0 \rightarrow \Omega$ maps a point \mathbf{X} in the reference configuration into its corresponding position in the current configuration, denoted by \mathbf{x} , such that $\varphi(\mathbf{X}) = \mathbf{x}$. Further, we define the deformation gradient tensor field \mathbf{F} as

$$\mathbf{F} := \frac{\partial\varphi}{\partial\mathbf{X}}(\mathbf{X}). \quad (2.1)$$

Without loss of generality, we decompose the displacement field \mathbf{u} as a sum of an affine transformation and a fluctuation field

$$\mathbf{u}(\mathbf{X}) = \bar{\mathbf{U}}\hat{\mathbf{X}} + \tilde{\mathbf{u}}, \quad (2.2)$$

where $\bar{\mathbf{U}} \in \mathcal{V}_{\bar{\mathbf{U}}} = \text{Sym}_n$ (space of $(n \times n)$ symmetric matrices), $\tilde{\mathbf{u}} : \Omega_0 \rightarrow \mathbb{R}^3$ is the fluctuation field, and $\hat{\mathbf{X}} := \mathbf{X} - \mathbf{X}_0$, with \mathbf{X}_0 a point in the reference configuration. The case where the macroscopic strain $\bar{\mathbf{U}}$ is given has been widely studied, with a remarkable theoretical approach adopted by De Souza Neto & Feijóo (2006) and Perić et al. (2011), where they develop the variational formulation of the problem and analyze different kinematical constraints on the fluctuation term, needed to make the problem well-posed; in contrast, note that here both $\bar{\mathbf{U}}$ and $\tilde{\mathbf{u}}$ are unknowns of the problem. As $\bar{\mathbf{U}}$ is a variable of the problem, the affine transformation can capture a scaling, shear and/or rotation of the RVE; however,

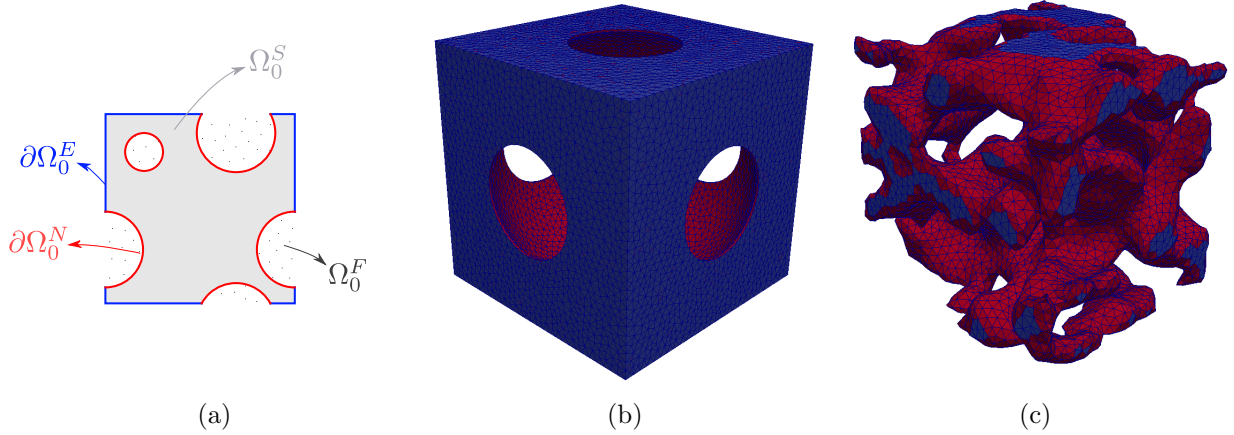


Figure 1: (a) 2D schematic of the ref. configuration of a periodic foam-like material RVE. In gray, the solid domain, while in blue and red, its bounding and inner boundaries, respectively. The colors in (b) and (c) are consistent with this definition. (b) Mesh of the spherical alveolar model, representing a spherical alveolus in the parenchyma. (c) Mesh of the image-based alveolar model, obtained by micro-CT images of rat lung parenchyma. For further details, refer to section 3.

we assume the pore pressure does not produce rotations, which is the reason why $\bar{\mathbf{U}}$ is symmetric. The explanation of this lies in the polar decomposition theorem, that states the deformation gradient can be decomposed uniquely as the product of two tensors: an orthogonal one, that corresponds to a rotation, and a symmetric one, that describes the deformation. Then, the purpose of enforcing $\bar{\mathbf{U}}$ to be symmetric is to capture only the component of deformation. For the fluctuation field, as done in Perić et al. (2011) and De Souza Neto & Feijóo (2006), we study the implications of different kinematical constraints, which corresponds to define suitable spaces $\mathcal{V}_{\tilde{\mathbf{u}}}$ such that $\tilde{\mathbf{u}} \in \mathcal{V}_{\tilde{\mathbf{u}}}$.

We model the mechanical behavior of the RVE using a variational approach, where we assume that the solid phase of the microstructure follows an incompressible hyperelastic behavior that is driven by the pore pressure. Within this framework, we define the internal energy of deformation by

$$\Pi_{\text{int}}(\bar{\mathbf{U}}, \tilde{\mathbf{u}}, p) = \int_{\Omega_0^S} \psi(\mathbf{F}, p) dV, \quad (2.3)$$

with

$$\psi(\mathbf{F}, p) := \psi_{\text{iso}}(\mathbf{F}) - p(J - 1) \quad , \quad \mathbf{F} = \mathbf{I} + \bar{\mathbf{U}} + \nabla_0 \tilde{\mathbf{u}}, \quad (2.4)$$

where p represents a Lagrange multiplier field needed to enforce the incompressibility condition in the formulation, $\psi(\mathbf{F}, p)$ is the strain energy density function of the incompressible solid, $\psi_{\text{iso}}(\mathbf{F})$ characterizes its isochoric response and $J := \det \mathbf{F}$. The external potential energy is defined as

$$\Pi_{\text{ext}}(\bar{\mathbf{U}}, \tilde{\mathbf{u}}) = -p_0 V^F, \quad (2.5)$$

where p_0 is the pore pressure exerted by the fluid, and $V^F := |\Omega^F|$ the current fluid volume. We note that, as the traction induced by the pore pressure on the inner boundary of the solid depends on the current configuration, and therefore on the deformation mapping, it cannot be always included in the potential energy as it may not derive from a potential density. In our case, we can include it because the fluid domain is enclosed by a surface (Bonet & Wood, 1997), composed by the inner boundary of the solid $\partial\Omega_0^N$ and the external boundary of the pores. As in the present work we are not interested in the fluid response, we impose the displacement to be zero ($\mathbf{u} = \mathbf{0}$) in the external boundary of the pores, so in the stationarity conditions the only relevant term associated to p_0 is

$$\begin{aligned} D_{\delta\mathbf{u}}\Pi_{\text{ext}}(\mathbf{u}) &= \int_{\partial\Omega_0^N} p_0 J \mathbf{F}^{-T} \mathbf{N} \cdot \delta\mathbf{u} \, dS \\ &= \int_{\partial\Omega_0^N} p_0 J \mathbf{F}^{-T} \mathbf{N} \cdot (\delta\bar{\mathbf{U}} \hat{\mathbf{X}} + \delta\tilde{\mathbf{u}}) \, dS, \end{aligned} \quad (2.6)$$

which is expressed as an integral on the solid inner boundary $\partial\Omega_0^N$, and where \mathbf{N} is the normal to the boundaries in the reference configuration.

Based on the definitions above, we express the total potential energy as

$$\Pi_{\text{tot}} := \Pi_{\text{int}} + \Pi_{\text{ext}}. \quad (2.7)$$

Then, from the Principle of stationary potential energy, we find the variational equations needed for the RVE equilibrium, starting with the stationary condition of $\tilde{\mathbf{u}}$

$$\begin{aligned} D_{\delta\tilde{\mathbf{u}}}\Pi_{\text{tot}}(\bar{\mathbf{U}}, \tilde{\mathbf{u}}, p) &= \int_{\partial\Omega_0^E} \bar{\mathbf{P}} \mathbf{N} \cdot \delta\tilde{\mathbf{u}} \, dS - \int_{\Omega_0^S} (\nabla_0 \cdot \bar{\mathbf{P}}) \cdot \delta\tilde{\mathbf{u}} \, dV \\ &+ \int_{\partial\Omega_0^N} (\bar{\mathbf{P}} \mathbf{N} + p_0 J \mathbf{F}^{-T} \mathbf{N}) \cdot \delta\tilde{\mathbf{u}} \, dS = 0 \quad \forall \delta\tilde{\mathbf{u}} \in \mathcal{V}_{\tilde{\mathbf{u}}}, \end{aligned} \quad (2.8)$$

with $\bar{\mathbf{P}}$ the first Piola-Kirchhoff stress tensor

$$\bar{\mathbf{P}}(\mathbf{F}, p) = \frac{d\psi}{d\mathbf{F}}(\mathbf{F}, p) = \frac{\partial\psi_{\text{iso}}}{\partial\mathbf{F}}(\mathbf{F}) - p J \mathbf{F}^{-T}. \quad (2.9)$$

Then, from Equation (2.8) we can deduce

$$\nabla_0 \cdot \bar{\mathbf{P}} = \mathbf{0} \quad \text{in } \Omega_0^S, \quad (2.10)$$

$$\bar{\mathbf{P}} \mathbf{N} = -p_0 J \mathbf{F}^{-T} \mathbf{N} \quad \text{on } \partial\Omega_0^N, \quad (2.11)$$

the missing relation for $\partial\Omega_0^E$ depends on the kinematical constraint for $\tilde{\mathbf{u}}$, and it will be analyzed in the next section.

The stationarity with respect to $\bar{\mathbf{U}}$ yields

$$D_{\delta\bar{\mathbf{U}}}\Pi_{\text{tot}}(\bar{\mathbf{U}}, \tilde{\mathbf{u}}, p) = \int_{\Omega_0^S} \bar{\mathbf{P}} : \nabla_0(\delta\bar{\mathbf{U}} \hat{\mathbf{X}}) dV + \int_{\partial\Omega_0^N} p_0 J \mathbf{F}^{-T} \mathbf{N} \cdot \delta\bar{\mathbf{U}} \hat{\mathbf{X}} dS = 0 \quad \forall \delta\bar{\mathbf{U}} \in \mathcal{V}_{\bar{\mathbf{U}}}, \quad (2.12)$$

however, noting that $\bar{\mathbf{U}}$ does not depend on \mathbf{X} , the first term can be expressed as

$$\int_{\Omega_0^S} \bar{\mathbf{P}} : \nabla_0(\delta\bar{\mathbf{U}} \hat{\mathbf{X}}) dV = \int_{\Omega_0^S} \bar{\mathbf{P}} : \delta\bar{\mathbf{U}} dV = \int_{\Omega_0^S} \bar{\mathbf{P}} dV : \delta\bar{\mathbf{U}}, \quad (2.13)$$

then,

$$D_{\delta\bar{\mathbf{U}}}\Pi_{\text{tot}}(\bar{\mathbf{U}}, \tilde{\mathbf{u}}, p) = \left[\int_{\Omega_0^S} \bar{\mathbf{P}} dV + \int_{\partial\Omega_0^N} p_0 J \mathbf{F}^{-T} \mathbf{N} \otimes \hat{\mathbf{X}} dS \right] : \delta\bar{\mathbf{U}} = 0 \quad \forall \delta\bar{\mathbf{U}} \in \mathcal{V}_{\bar{\mathbf{U}}}. \quad (2.14)$$

The macroscopic first Piola-Kirchhoff stress tensor in the solid domain is defined as

$$\langle \bar{\mathbf{P}} \rangle := \frac{1}{|\Omega_0^S|} \int_{\Omega_0^S} \bar{\mathbf{P}} dV, \quad (2.15)$$

and replacing it in Equation (2.14)

$$\left[|\Omega_0^S| \langle \bar{\mathbf{P}} \rangle + \int_{\partial\Omega_0^N} p_0 J \mathbf{F}^{-T} \mathbf{N} \otimes \hat{\mathbf{X}} dS \right] : \delta\bar{\mathbf{U}} = 0 \quad \forall \delta\bar{\mathbf{U}} \in \mathcal{V}_{\bar{\mathbf{U}}}, \quad (2.16)$$

which, due to the symmetry of $\bar{\mathbf{U}}$, implies the following equation

$$|\Omega_0^S| \left(\langle \bar{\mathbf{P}} \rangle + \langle \bar{\mathbf{P}} \rangle^T \right) = - \int_{\partial\Omega_0^N} (p_0 J \mathbf{F}^{-T} \mathbf{N} \otimes \hat{\mathbf{X}}) + (\hat{\mathbf{X}} \otimes p_0 J \mathbf{F}^{-T} \mathbf{N}) dS, \quad (2.17)$$

that can be interpreted as a relation between the macroscopic first Piola-Kirchhoff stress tensor and the pressure applied on the inner boundary. However, as the deformation gradient tensor depends on $\bar{\mathbf{U}}$ and $\tilde{\mathbf{u}}$, this relation is coupled with the rest of the equations, and the macroscopic stress cannot be obtained *a priori*.

For the Lagrange multiplier p , the stationarity corresponds to

$$D_{\delta p}\Pi_{\text{tot}}(\bar{\mathbf{U}}, \tilde{\mathbf{u}}, p) = \int_{\Omega_0^S} \delta p (J - 1) dV = 0 \quad \forall \delta p \in \mathcal{V}_p, \quad (2.18)$$

which implies the incompressibility of the solid, that in terms of $J(\mathbf{F})$ is

$$J(\mathbf{F}) = 1 \quad \text{in } \Omega_0^S. \quad (2.19)$$

We note that in the framework of poromechanics and in the mixture theory, the incompressibility has also been related to the true density of the constituents (the mass of a constituent per unit volume of that constituent). Then, if a constituent is incompressible, its true density is constant, and if the mixture is incompressible, the true densities of all constituents are constant (Bowen, 1980, 1982).

2.1. Kinematical constraints

To complete the problem, a suitable space for the displacement fluctuation must be selected. We will discuss three options commonly adopted:

- (i) Kinematic uniform boundary condition (KUUBC): The boundary displacement fluctuation vanishes

$$\mathcal{V}_{\tilde{\mathbf{u}}} = \mathcal{V}_{\tilde{\mathbf{u}}}^{\text{kubc}} := \{\tilde{\mathbf{u}} \in H^1(\Omega_0^S) \mid \tilde{\mathbf{u}}(\mathbf{X}) = \mathbf{0} \quad \forall \mathbf{X} \text{ on } \partial\Omega_0^E\}, \quad (2.20)$$

$$\mathcal{V}_p = \mathcal{V}_p^{\text{kubc}} := L^2(\Omega_0^S). \quad (2.21)$$

- (ii) Periodic displacement boundary condition (PBC): Used to describe materials with periodic microstructure, here it is assumed that the boundary $\partial\Omega_0^E$ is periodic, so there exists pairs $\{\mathbf{X}^+, \mathbf{X}^-\}$ that relate the coordinates of two periodic faces. In this case

$$\mathcal{V}_{\tilde{\mathbf{u}}} = \mathcal{V}_{\tilde{\mathbf{u}}}^{\text{pbc}} := \{\tilde{\mathbf{u}} \in H^1(\Omega_0^S) \mid \tilde{\mathbf{u}}(\mathbf{X}^+) = \tilde{\mathbf{u}}(\mathbf{X}^-) \quad \forall \text{ pairs } \{\mathbf{X}^+, \mathbf{X}^-\}\}, \quad (2.22)$$

$$\mathcal{V}_p = \mathcal{V}_p^{\text{pbc}} := \{p \in L^2(\Omega_0^S) \mid p(\mathbf{X}^+) = p(\mathbf{X}^-) \quad \forall \text{ pairs } \{\mathbf{X}^+, \mathbf{X}^-\}\}. \quad (2.23)$$

As in $\partial\Omega_0^E$ the fluctuation $\tilde{\mathbf{u}}$ is periodic, from the first term in Equation (2.8)

$$\int_{\partial\Omega_0^E} \bar{\mathbf{P}}\mathbf{N} \cdot \delta\tilde{\mathbf{u}} \, dS = 0 \quad \forall \delta\tilde{\mathbf{u}} \in \mathcal{V}_{\tilde{\mathbf{u}}}, \quad (2.24)$$

and we see the periodicity in the fluctuation term implies the anti-periodicity of the traction $\bar{\mathbf{P}}\mathbf{N}$ on the external boundary

$$(\bar{\mathbf{P}}\mathbf{N})^+ = -(\bar{\mathbf{P}}\mathbf{N})^- \quad \text{on } \partial\Omega_0^E, \quad (2.25)$$

where $(\bar{\mathbf{P}}\mathbf{N})^+$ and $(\bar{\mathbf{P}}\mathbf{N})^-$ correspond to the traction in the periodic pairs \mathbf{X}^+ and \mathbf{X}^- , respectively.

- (iii) Uniform traction boundary condition (also known as stress uniform boundary conditions, SUBC): the traction is uniform in the boundary, with the first Piola-Kirchhoff stress tensor constant. This condition can be enforced with a Lagrange multiplier (Javili et al., 2017), adding a term in the external potential energy

$$\Pi_{\text{ext}}(\bar{\mathbf{U}}, \tilde{\mathbf{u}}, \boldsymbol{\lambda}) = p_0 V^E + \boldsymbol{\lambda} : \int_{\partial\Omega_0^E} \tilde{\mathbf{u}} \otimes \mathbf{N} \, dS, \quad (2.26)$$

where $\boldsymbol{\lambda} \in \mathbf{M}_3$ is the Lagrange multiplier, with \mathbf{M}_n the space of all $(n \times n)$ matrices. Note that $\boldsymbol{\lambda}$ is outside the integral because it is a constant tensor, that does not depend

on \mathbf{X} , however, this term could also be written as $\int_{\partial\Omega_0^E} \boldsymbol{\lambda} \mathbf{N} \cdot \tilde{\mathbf{u}} \, dS$. Then, the stationary condition of $\tilde{\mathbf{u}}$ yields

$$\begin{aligned} D_{\delta\tilde{\mathbf{u}}}\Pi_{\text{tot}}(\bar{\mathbf{U}}, \tilde{\mathbf{u}}, p, \boldsymbol{\lambda}) &= \int_{\partial\Omega_0^E} (\bar{\mathbf{P}}\mathbf{N} - \boldsymbol{\lambda}\mathbf{N}) \cdot \delta\tilde{\mathbf{u}} \, dS - \int_{\Omega_0^S} (\nabla_0 \cdot \bar{\mathbf{P}}) \cdot \delta\tilde{\mathbf{u}} \, dV \\ &+ \int_{\partial\Omega_0^N} (\bar{\mathbf{P}}\mathbf{N} + p_0 J \mathbf{F}^{-T} \mathbf{N}) \cdot \delta\tilde{\mathbf{u}} \, dS = 0 \quad \forall \delta\tilde{\mathbf{u}} \in \mathcal{V}_{\tilde{\mathbf{u}}}, \end{aligned} \quad (2.27)$$

from which we obtain Equations (2.10), (2.11) and the uniform traction condition

$$\bar{\mathbf{P}}\mathbf{N} = \boldsymbol{\lambda}\mathbf{N} \quad \text{on } \partial\Omega_0^E. \quad (2.28)$$

The stationarity with respect to $\bar{\mathbf{U}}$ is equal to the developed in the previous section, and with respect to $\boldsymbol{\lambda}$ is

$$D_{\delta\boldsymbol{\lambda}}\Pi_{\text{tot}}(\tilde{\mathbf{u}}, \boldsymbol{\lambda}) = \delta\boldsymbol{\lambda} : \int_{\partial\Omega_0^E} \tilde{\mathbf{u}} \otimes \mathbf{N} \, dS = 0 \quad \forall \delta\boldsymbol{\lambda} \in \mathbf{M}_3, \quad (2.29)$$

which implies

$$\int_{\partial\Omega_0^E} \tilde{\mathbf{u}} \otimes \mathbf{N} \, dS = \mathbf{0}. \quad (2.30)$$

This suggests the definition of the space $\mathcal{V}_{\tilde{\mathbf{u}}}^{\text{subc}}$ as

$$\mathcal{V}_{\tilde{\mathbf{u}}}^{\text{subc}} := \{\tilde{\mathbf{u}} \in H^1(\Omega_0^S) \mid \int_{\partial\Omega_0^E} \tilde{\mathbf{u}} \otimes \mathbf{N} \, dS = \mathbf{0}\}. \quad (2.31)$$

Then, the spaces $\mathcal{V}_{\tilde{\mathbf{u}}}^{\text{kubc}}$, $\mathcal{V}_{\tilde{\mathbf{u}}}^{\text{bbc}}$ and $\mathcal{V}_{\tilde{\mathbf{u}}}^{\text{subc}}$ can be related as

$$\mathcal{V}_{\tilde{\mathbf{u}}}^{\text{kubc}} \subset \mathcal{V}_{\tilde{\mathbf{u}}}^{\text{bbc}} \subset \mathcal{V}_{\tilde{\mathbf{u}}}^{\text{subc}}. \quad (2.32)$$

The first relation is direct, due to the vanishing of the boundary fluctuations in the KUBC case. For the periodic case, the condition $\int_{\partial\Omega_0^E} \tilde{\mathbf{u}} \otimes \mathbf{N} \, dS = \mathbf{0}$ is accomplished due to the periodicity of $\tilde{\mathbf{u}}$ and the anti-periodicity of \mathbf{N} .

For p , in this case

$$\mathcal{V}_p = \mathcal{V}_p^{\text{subc}} = L^2(\Omega_0^S). \quad (2.33)$$

Finally, we can express the strong form of the problem as: Given p_0 , find $\bar{\mathbf{U}} \in \mathcal{V}_{\bar{\mathbf{U}}}$, $\tilde{\mathbf{u}} \in \mathcal{V}_{\tilde{\mathbf{u}}}$ and $p \in \mathcal{V}_p$, such that

$$\left. \begin{aligned} \nabla_0 \cdot \bar{\mathbf{P}}(\mathbf{F}, p) &= \mathbf{0} \\ \bar{\mathbf{P}}(\mathbf{F}, p)\mathbf{N} &= -p_0 J \mathbf{F}^{-T} \mathbf{N} \\ J(\mathbf{F}) &= 1 \\ \mathbf{F} &= \mathbf{I} + \bar{\mathbf{U}} + \nabla_0 \tilde{\mathbf{u}} \end{aligned} \right\} \begin{array}{l} \text{in } \Omega_0^S, \\ \text{on } \partial\Omega_0^N, \\ \text{in } \Omega_0^S, \\ \text{in } \Omega_0^S, \end{array} \quad (2.34)$$

$$|\Omega_0^S| \left(\langle \bar{\mathbf{P}} \rangle + \langle \bar{\mathbf{P}} \rangle^T \right) = - \int_{\partial\Omega_0^N} (p_0 J \mathbf{F}^{-T} \mathbf{N} \otimes \hat{\mathbf{X}}) + (\hat{\mathbf{X}} \otimes p_0 J \mathbf{F}^{-T} \mathbf{N}) \, dS.$$

Plus,

$$\begin{aligned} (\bar{\mathbf{P}}\mathbf{N})^+ &= -(\bar{\mathbf{P}}\mathbf{N})^- \quad \text{on } \partial\Omega_0^E \text{ for PBC,} \\ \bar{\mathbf{P}}(\mathbf{F}, p)\mathbf{N} &= \boldsymbol{\lambda}\mathbf{N} \quad \text{on } \partial\Omega_0^E \text{ for SUBC, with } \boldsymbol{\lambda} \in \mathbb{M}_3 \text{ a variable of the problem.} \end{aligned}$$

2.2. The deformation-driven case

For comparison purposes, we also consider the case where macroscopic deformation alone drives the response of the porous RVE. In this case, we set the pore pressure equal to zero ($p_0 = 0$) and apply an equivalent macroscopic strain, which is obtained from the solution to the pressure-driven case. For the displacement fluctuation, the boundary conditions are analogous to the pressure-driven setting. Then, the strong form of the deformation-driven problem reads: Given a macroscopic deformation $\bar{\mathbf{U}}$, find $\tilde{\mathbf{u}} \in \mathcal{V}_{\tilde{u}}$ and $p \in \mathcal{V}_p$, such that

$$\left. \begin{aligned} \nabla_0 \cdot \bar{\mathbf{P}}(\mathbf{F}, p) &= \mathbf{0} && \text{in } \Omega_0^S, \\ \bar{\mathbf{P}}(\mathbf{F}, p)\mathbf{N} &= \mathbf{0} && \text{on } \partial\Omega_0^N, \\ J(\mathbf{F}) &= 1 && \text{in } \Omega_0^S, \\ \mathbf{F} &= \mathbf{I} + \bar{\mathbf{U}} + \nabla_0 \tilde{\mathbf{u}} && \text{in } \Omega_0^S. \end{aligned} \right\} \quad (2.35)$$

In addition, we consider

$$\begin{aligned} (\bar{\mathbf{P}}\mathbf{N})^+ &= -(\bar{\mathbf{P}}\mathbf{N})^- \quad \text{on } \partial\Omega_0^E \text{ for PBC,} \\ \bar{\mathbf{P}}(\mathbf{F}, p)\mathbf{N} &= \boldsymbol{\lambda}\mathbf{N} \quad \text{on } \partial\Omega_0^E \text{ for SUBC, with } \boldsymbol{\lambda} \in \mathbb{M}_3 \text{ a variable of the problem.} \end{aligned}$$

3. Numerical Examples

The proposed variational framework can be applied to the study of different kinds of pressurized foams. In this section, we will focus on the behavior of the lung tissue, a pressurized biological foam, through two examples: first, a spherical alveolar model, representing a single spherical alveolus inside a box, and then an image-based alveolar model, obtained from micro-CT images of rat lung parenchyma (Concha & Hurtado, 2020). The objective of these models is to observe how simplifications on the geometry affect the micromechanical response, such as the stress distribution within the RVE, or the presence of local phenomena. In both cases two load patterns will be analyzed, first a pressure-driven RVE, with a uniform pore pressure in the cavity and with the macroscopic strain as a variable of the problem, and then in a deformation-driven setting, removing the pore pressure and applying an equivalent macroscopic strain. Both loading conditions intend to represent, in an approximate way, physiological conditions in the pulmonary tissue. The pressure-driven model resembles the tissue conditions under mechanical ventilation, where the respiratory muscles are passive and the pressure generated by the ventilator drives the air into the lungs (Mauri et al., 2017),

and the deformation-driven mimics spontaneous breathing, where the respiratory muscles have an active role. In all cases, we will compare the three kinematical constraints (KUBC, PBC and SUBC) in terms of the stress distributions.

For the lung parenchyma mechanical behavior, we select an incompressible neo-Hookean strain energy function, with an elastic modulus set to $E = 95$ kPa according to the values reported by Perlman & Wu (2014), which is equivalent to $\mu = \frac{E}{2(1+\nu)} = 31.7$ kPa, using a Poisson ratio $\nu = 0.5$. It is worth noting that other phenomenological strain energy functions have been studied for the representation of the behavior of lung parenchyma in the literature (Bel-Brunon et al., 2014; Birzle et al., 2019; Birzle & Wall, 2019). However, in this work we choose the neo-Hookean model to minimize the number of material parameters and the non-linearity of the material model, and concentrate on the effect of boundary conditions and microstructural geometry. The RVE is loaded using a positive pore pressure ranging from $p_0 = 0$ to 1.962 kPa. The numerical simulations were carried out using the FEniCS library for finite element computations (Logg et al., 2012). To account for the incompressible behavior of the solid phase, we considered a mixed FE formulation that employs P_2 - P_1 Taylor-Hood tetrahedral elements.

3.1. Spherical alveolar model

In the literature, the complex lung parenchyma microstructure has been simplified using polyhedral representations (Concha et al., 2018; Fung, 1988; Koshiyama & Wada, 2015; Roth et al., 2017; Warren & Kraynik, 1997). However, as in this work the main objective of the numerical simulations is to illustrate the application of the model described in the previous section, and not necessarily present a detailed study of the tissue behavior, here we will use a geometry consisting of a spherical cavity embedded in a homogeneous matrix, that represents a large spherical alveolus. The mesh was constructed using GMSH (Geuzaine & Remacle, 2009), with special care to make the external boundary periodic (requisite for the PBC); specifically, it consists in a cube of edge size $122.5 \mu\text{m}$ (the same size as the image-based RVE that will be studied) with an internal spherical cavity that intersects the cube boundaries, as shown in Figure 1b. The cavity radius is such that the porosity of the RVEs of the spherical and image-based alveolar models be similar, with the porosity in the reference configuration defined as $f_0 := |\Omega_0^F|/|\Omega_0|$, which in this case gives 63.24% (versus 63.22% for the image-based RVE of figure 1c). We remark that, while both geometries have similar porosity, the single alveolus model considers a uniform smooth cavity, which is clearly different from the intricate microstructure observed in micro-CT images of alveolar tissue. A measure of this difference is the surface-to-volume ratio, that if defined as the area of the inner surface $\partial\Omega_0^N$ divided by the volume of gas in the RVE, gives a value of $0.0356 \mu\text{m}^{-1}$ for the spherical model and $0.1032 \mu\text{m}^{-1}$ for the image-based case (see Section 3.2).

To compare the performance of the different kinematical constraints, we use two scalar stress measures: the hydrostatic stress, related with the first invariant of the Cauchy stress

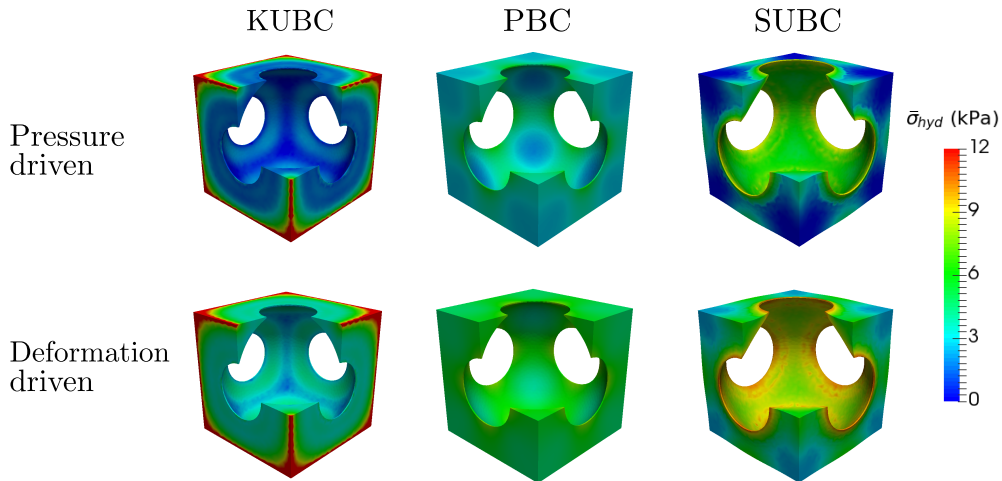


Figure 2: Hydrostatic stress field in the spherical alveolar model, plotted in the current configuration.

tensor,

$$\bar{\sigma}_{\text{hyd}} := \frac{1}{3} \text{trace}(\bar{\sigma}), \quad (3.1)$$

where $\bar{\sigma} = J^{-1} \bar{\mathbf{P}} \mathbf{F}^T$, and the von Mises stress,

$$\bar{\sigma}_{\text{VM}} := \sqrt{\frac{3}{2} \bar{\sigma}_{\text{dev}} : \bar{\sigma}_{\text{dev}}}, \quad (3.2)$$

that is related to shear stresses, and where the deviatoric component of the stress tensor is

$$\bar{\sigma}_{\text{dev}} := \bar{\sigma} - \bar{\sigma}_{\text{hyd}} \mathbf{I}. \quad (3.3)$$

From these definitions, we note that the hydrostatic and the von Mises stress quantify two independent and orthogonal components of the Cauchy stress tensor.

Figures 2 and 3 show the hydrostatic and von Mises stress for a pore pressure of 1.962 kPa, respectively. As the Cauchy stress tensor is defined in the current configuration, in these Figures the quantities are plotted in the deformed state. For the hydrostatic stress, the RVE exhibits a response that depends on the kinematical constraint and the type of loading. While for the KUBC there are peak values near the cube edges, in the SUBC there are peaks near the sphere edges (where it intersects the cube faces), especially noticeable in the deformation-driven case. For the von Mises stress, the distribution is independent of the type of loading. However, it depends on the kinematical constraint: in the KUBC there are smaller values, in the SUBC there are peaks in the sphere edges and the PBC response is similar to the SUBC but without these peak values.

The stress distributions plotted in the current configuration allow observing the distributions, if there are peak values and where they are located, however, for a more detailed

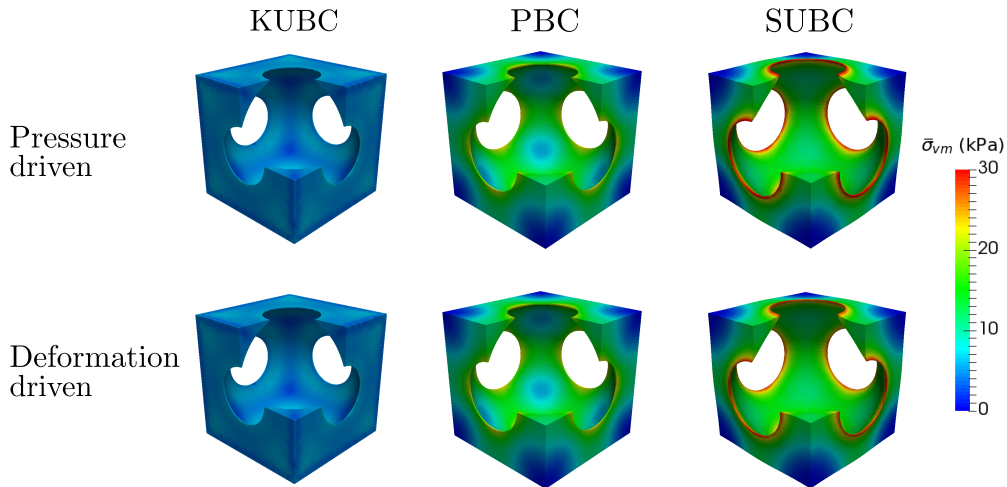


Figure 3: Von Mises stress field in the spherical alveolar model, plotted in the current configuration.

comparison, in Figure 4 the frequency distributions of the hydrostatic and von Mises stress are presented. To facilitate the comparison, in these figures the curves were done using the `gaussian_kde` function available in `SciPy` (Virtanen et al., 2020), which produce a kernel-density estimate using Gaussian kernels. The results show that for the hydrostatic stress, the three kinematical constraints produce different distributions, but for each case, when the macrostrain is given instead of applying a pore pressure (i.e., deformation-driven instead of pressure-driven), there is a shift in the distributions, with higher values but the same shape. For the von Mises stress, the distribution in the PBC and SUBC are similar, in agreement with the observed in Figure 3, while the KUBC exhibits lower and more concentrated values. Additionally, for the KUBC and PBC the distribution is indistinguishable for both loadings (pressure-driven in solid lines, deformation-driven in dashed lines), while for the SUBC there is a slight difference between 10 and 15 kPa, that is not noticeable in the plots of Figure 3.

3.2. Image-based alveolar model

For the image-based alveolar model, a cuboid RVE of edge size $122.5 \mu\text{m}$ is selected from micro-CT images of rat lung parenchyma previously reported by our group (Concha et al., 2018; Sarabia-Vallejos et al., 2019). The RVE preserves the morphological features of the alveolated tissue; however, due to the natural heterogeneities the resulting mesh is not periodic, hindering the straight use of PBC. To overcome this issue different methods have been proposed, for example Pahr & Zysset (2008) used a perfectly periodic mirrored mesh of cancellous bone (obtained by reflecting successively the original mesh in the x , y and z directions). To avoid the need of matching meshes on opposite RVE boundaries, Larson et al. (2011) weakly imposed the fluctuation periodicity (and traction anti-periodicity), and Nguyen et al. (2012) developed a method based on polynomial interpolation of the displacement in the boundaries. In this paper, following the straightforward approach of the mirrored mesh, the original RVE (Figure 1c) is reflected, obtaining the geometry shown in Figure 5, a cube of edge size $245 \mu\text{m}$, which is easy to obtain but that is not a completely

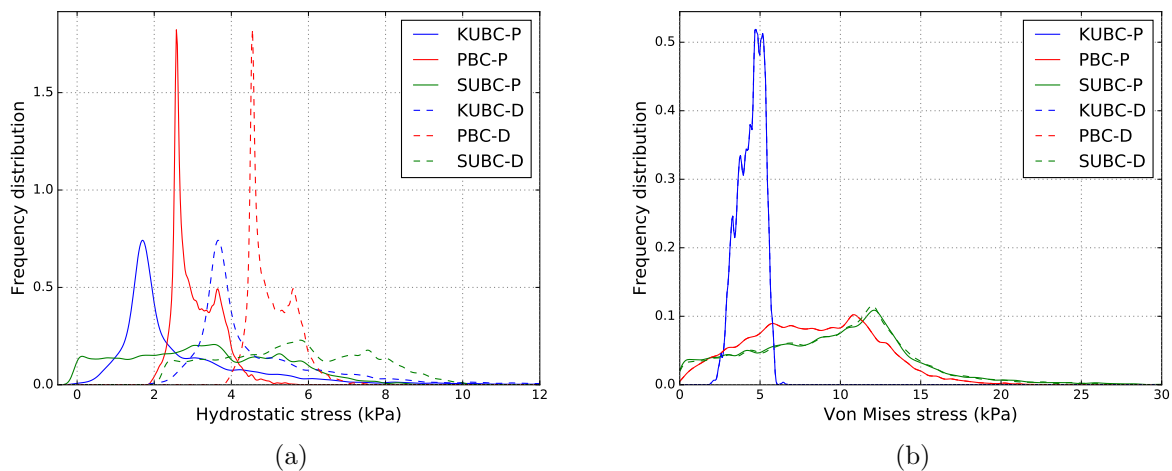


Figure 4: Spherical alveolar model, distributions for (a) hydrostatic stress, and (b) von Mises stress. The values depend on the kinematical constraint selected: KUBC (blue), PBC (red) and SUBC (green), and in the type of loading: pressure-driven in solid lines, deformation-driven in dashed lines. For each kinematical constraint, the removal of the pore pressure and application of an equivalent macrostrain, produces a shift in the hydrostatic stress, while the von Mises stress remains constant with the KUBC and PBC, and has slight differences with the SUBC.

realistic structure and has eight times the number of elements of the original mesh.

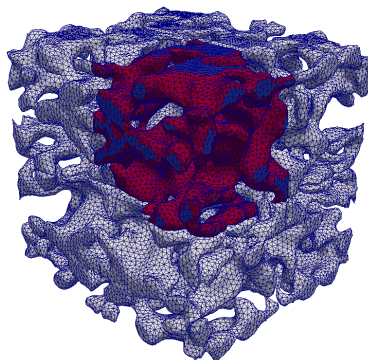


Figure 5: The mesh of the image-based alveolar model obtained by micro-CT images is not periodic (due to natural heterogeneities in the tissue), so in order to apply the PBC the original mesh (in red) is reflected successively in the x , y and z directions, obtaining a perfectly periodic mesh (in gray).

Analogous to the spherical alveolar model, we plot the hydrostatic and von Mises stress distributions, which are shown in Figures 6 and 7. In this case, we see that for both measures, the stress values are similar with the KUBC, PBC and SUBC constraints, except for some values in the exterior boundary, particularly around the upper right corner of the deformed RVE, where a thin “bar” of tissue has higher stress values with the SUBC and

lower values with the KUBC.

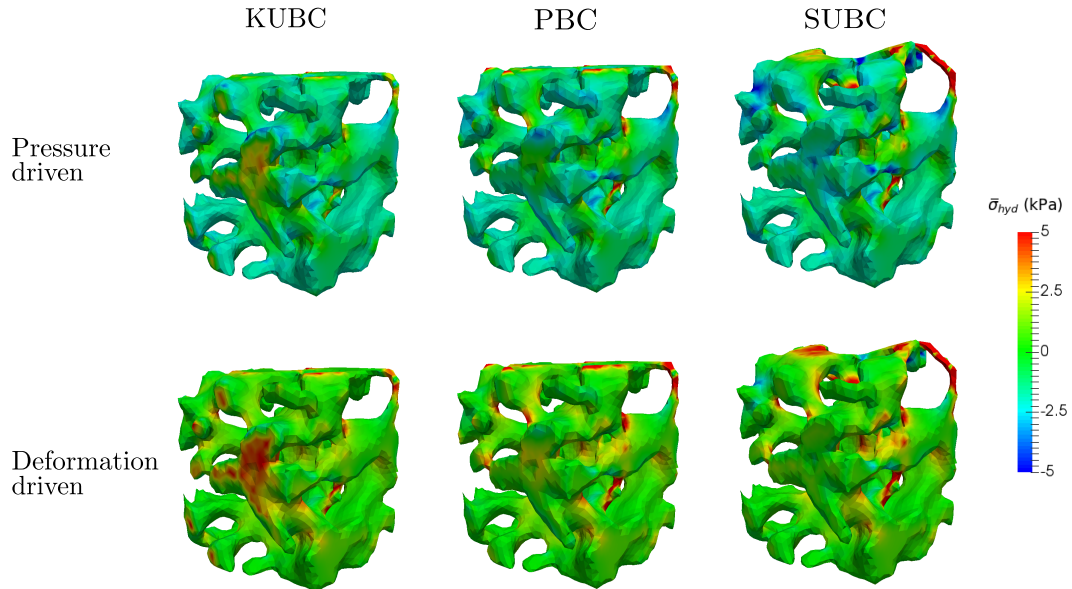


Figure 6: Hydrostatic stress field in the image-based alveolar model, plotted in the current configuration.

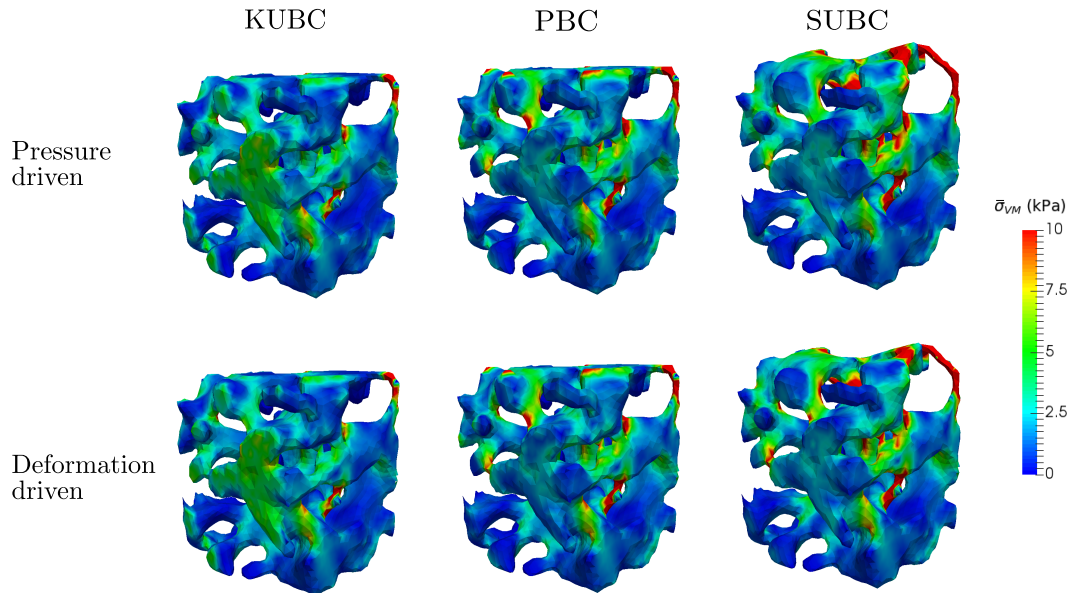


Figure 7: Von Mises stress field in the image-based alveolar model, plotted in the current configuration.

Consistent with the plots of Figure 6, the results reported in Figure 8a show that the hydrostatic stress distributions are similar for the three kinematical constraints. In effect, in the pressure-driven case, the KUBC, PBC and SUBC models result in a peak that occurs

close to the pore pressure (1.96 kPa). Interestingly, in the deformation-driven case, the shape of the stress distributions are similar to those observed in the pressure-driven setting, only shifted towards the positive values with the peak occurring near 0 kPa. Regarding the von Mises stress, there are virtually no differences between the pressure- and deformation-driven cases, see Figure 8b. Further, all distributions are unimodal, with the KUBC and PBC giving similar values, and the SUBC slightly higher values.

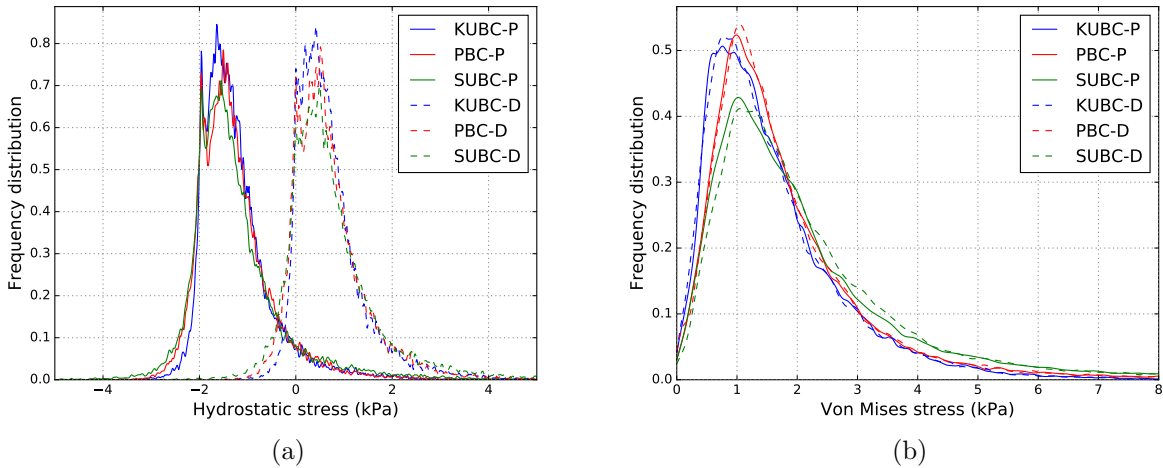


Figure 8: Image-based alveolar model, distributions for (a) hydrostatic stress, and (b) von Mises stress. The Figure shows the results with each kinematical constraint: KUBC (blue), PBC (red) and SUBC (green); and type of loading: pressure-driven in solid lines, deformation-driven in dashed lines. For both stress measures, the shape of the distributions is similar for the different kinematical constraints. Also, the removal of the pore pressure and application of an equivalent macrostrain, produces a shift in the hydrostatic stress, while the von Mises stress remains similar.

4. Discussion

In this work, we propose a variational framework for the micromechanical response of OCFs. We employ the framework in the analysis of the micromechanical behavior under pressure-driven conditions, where we consider a spherical alveolar and an image-based alveolar models to assess the stress distributions. For each geometry considered, three different boundary conditions were studied. One key conclusion is that both the hydrostatic and deviatoric stress distributions in the spherical alveolar model were highly dependent on the boundary condition assumed for the micromechanical analysis, see Figure 4. In effect, the peak values of the distributions did not coincide, and there was no clear trend in terms of modality of the distribution. In contrast, when looking at image-based alveolar model, all three boundary conditions resulted in virtually the same stress distribution, see Figure 8. In particular, the hydrostatic distribution displayed a bimodal shape, whereas the von Mises stress showed positively-skewed unimodal distribution. To facilitate a comparison between the spherical and image-based alveolar models, we have summarized the stress distributions

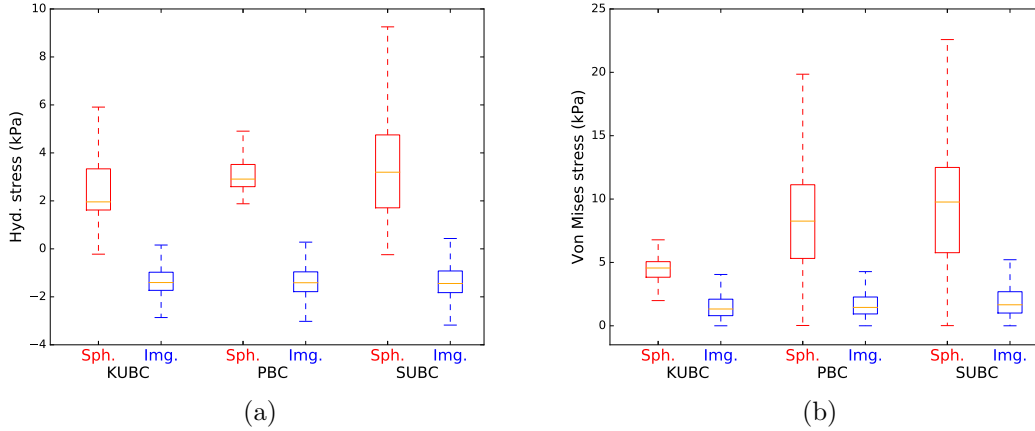


Figure 9: Comparison of the (a) hydrostatic and (b) von Mises stress distributions for the pressure-driven RVE, with the spherical and image-based alveolar models, in red and blue boxes, respectively. The boxes range from the lower (Q_1) to upper (Q_3) quartile values of the stress, with a line at the median. The whiskers extend from the boxes to show the range of the data. The upper whiskers extend to the last value less than $Q_3 + 1.5 \text{ IQR}$, while the lower whiskers to the first value greater than $Q_1 - 1.5 \text{ IQR}$, where $\text{IQR} = Q_3 - Q_1$ is the interquartile range. The outliers are not shown for clarity.

in terms of box and whisker plots, see Figure 9. We observe that in the case of image-based alveolar model, all boundary conditions lead to consistent stress distributions, which is not the case for the spherical model. We further note that the results for the image-based model are consistent with stress distributions reported in previous works, where alveolar geometries obtained from micro-CT images under varying levels of alveolar pressure were analyzed (Sarabia-Vallejos et al., 2019). In those simulations, boundary conditions were arbitrarily chosen, not based on theoretical grounds. The resulting hydrostatic and deviatoric stress distributions in that work are very similar in shape to those shown in Figure 8. Interestingly, in this work we have shown that in anatomical geometries, the conditions imposed on the boundary do not seem to play a key role in the micromechanical response. A possible explanation for this behavior is the random unstructured trabecular geometry of the alveolated pulmonary tissue, that quickly dissipates stress localizations that may arise at the boundaries of the RVE due to different conditions, see Figures 6 and 7. From these results, we conclude that, while two RVE may have similar macroscopic properties such as global porosity, their microstructural stresses can strongly differ. Further, stresses in randomly-structured RVEs do not seem affected by the boundary conditions, whereas highly structured RVEs do.

To understand the differences between formulations where either pressure or deformation is imposed, we consider models where boundary conditions are driven by a macroscopic deformation $\bar{\mathbf{U}}$ under zero pore pressure. The results in both the spherical and image-based alveolar models (Figures 4 and 8, respectively) show that the hydrostatic stress distributions are shifted between the pressure-driven and the deformation-driven cases, while the von Mises stress distributions remain the same. Interestingly, in the deformation-driven case

we observe that boundary conditions do affect the spherical model distribution of stress in a way similar to the pressure-driven case. However, the results for the deformation-driven image-based model show that the choice of boundary conditions does not influence the stress distribution, resembling the behavior observed in the pressure-driven case. We remark that the shift in the hydrostatic stresses in finite deformation poro-elasticity has been addressed by Idiart & Lopez-Pamies (2012), borrowing ideas from Julien et al. (2011) and Vincent et al. (2009). In their work, Idiart & Lopez-Pamies showed that stresses in an incompressible elastomeric solid with pressurized closed cavities can be expressed as

$$\bar{\mathbf{P}} = \tilde{\mathbf{P}} - p_0 J \mathbf{F}^{-T}, \quad (4.1)$$

where $\tilde{\mathbf{P}}$ corresponds to the first Piola-Kirchhoff stress tensor obtained from solving the same microstructure subject to an equivalent macroscopic strain and zero pore pressure, and p_0 corresponds to the pressure applied in the closed cavities. In the current configuration, Equation 4.1 is equivalent to adding a hydrostatic pressure term with magnitude p_0 to the Cauchy stress tensor, which explains the shift in the hydrostatic stress distribution. Since the cavity pressure effect only results in an isotropic tensor, the von Mises stress remains the same under this transformation. In Idiart & Lopez-Pamies (2012), to find the equivalent macroscopic strain, an additional equation is imposed, which is based on the traction-free condition on the external boundary, and consists in making zero the average of the first Piola-Kirchhoff stress tensor in the entire RVE (solid and fluid domain). Interestingly, under the same assumptions (a closed-cell composite and extending $\tilde{\mathbf{P}}$ to the fluid domain) and with some algebraic manipulations, this equation can be related to the stationary condition Equation (2.16), which is generated by considering the macroscopic strain as a variable of the problem. The relationship between pressure-driven and deformation-driven formulations has profound consequences on the modeling of free-breathing versus ventilated-breathing, for instance in the context of lung mechanical simulations (Hurtado et al., 2020; Patte et al., 2020, 2019; Tawhai & Lin, 2010).

The present work can be expanded in several directions. First, we note that the choice of a neo-Hookean strain energy function imposes an important limitation when studying OCFs, which may exhibit a strongly non-linear mechanical behavior (for lung parenchyma, see Bel-Brunon et al. (2014), Birzle et al. (2019), and Birzle & Wall (2019)). In this work we chose a simple constitutive law to isolate its effect on the results, allowing us to better focus on assessing the impact of boundary conditions and geometry on the RVE stress distribution and response. Future contributions should incorporate other constitutive relations that are specific to the material under analysis, and that may exhibit other type of mechanical behavior, e.g. viscoelastic and hysteretic response (West, 2012). This, in turn, may necessitate an extension of the current variational framework, which has been developed under the assumption of a material with hyperelastic response. Another limitation is the lack of experimental validation of the results obtained from numerical simulations. Micro-CT imaging combined with digital image correlation has been used to assess the deformation fields arising in bone samples under compressive loading (Dickinson et al., 2011), allowing for the validation of FE simulations of bone microstructures (Hambli, 2013). We note, however,

that the validation of pressurized porous materials may require more sophisticated setups that maintain the applied pressure in sealed samples, which may not be compatible with current micro-CT technologies.

Acknowledgements

This work was funded by the National Agency for Research and Development (ANID) of Chile through the grant FONDECYT Regular # 1180832.

References

- Altenbach, H., & Öchsner, A. (Eds.) (2010). *Cellular and porous materials in structures and processes*. Springer Science & Business Media.
- Bednarczyk, B. A., Aboudi, J., Arnold, S. M., & Sullivan, R. M. (2008). Analysis of Space Shuttle external tank spray-on foam insulation with internal pore pressure. *Journal of Engineering Materials and Technology, Transactions of the ASME, 130*. doi:10.1115/1.2969247.
- Bel-Brunon, A., Kehl, S., Martin, C., Uhlig, S., & Wall, W. A. (2014). Numerical identification method for the non-linear viscoelastic compressible behavior of soft tissue using uniaxial tensile tests and image registration - Application to rat lung parenchyma. *Journal of the Mechanical Behavior of Biomedical Materials, 29*, 360–374. doi:10.1016/j.jmbbm.2013.09.018.
- Biot, M. A. (1941). General theory of three-dimensional consolidation. *Journal of Applied Physics, 12*, 155–164. doi:10.1063/1.1712886.
- Birzle, A. M., Hobrack, S. M., Martin, C., Uhlig, S., & Wall, W. A. (2019). Constituent-specific material behavior of soft biological tissue: experimental quantification and numerical identification for lung parenchyma. *Biomechanics and Modeling in Mechanobiology, 18*, 1383–1400. doi:10.1007/s10237-019-01151-3.
- Birzle, A. M., & Wall, W. A. (2019). A viscoelastic nonlinear compressible material model of lung parenchyma - Experiments and numerical identification. *Journal of the Mechanical Behavior of Biomedical Materials, 94*, 164–175. doi:10.1016/j.jmbbm.2019.02.024.
- Bonet, J., & Wood, R. D. (1997). *Nonlinear continuum mechanics for finite element analysis*. Cambridge University Press. doi:10.1017/CB09780511755446.
- Bowen, R. M. (1980). Incompressible porous media models by use of the theory of mixtures. *International Journal of Engineering Science, 18*, 1129–1148.
- Bowen, R. M. (1982). Compressible porous media models by use of the theory of mixtures. *International Journal of Engineering Science, 20*, 697–735.
- Carniel, T. A., Klahr, B., & Fancello, E. A. (2019). On multiscale boundary conditions in the computational homogenization of an RVE of tendon fascicles. *Journal of the Mechanical Behavior of Biomedical Materials, 91*, 131–138. doi:10.1016/j.jmbbm.2018.12.003.
- Chapelle, D., & Moireau, P. (2014). General coupling of porous flows and hyperelastic formulations - From thermodynamics principles to energy balance and compatible time schemes. *European Journal of Mechanics, B/Fluids, 46*, 82–96. doi:10.1016/j.euromechflu.2014.02.009.
- Concha, F., & Hurtado, D. E. (2020). Upscaling the poroelastic behavior of the lung parenchyma: A finite-deformation micromechanical model. *Journal of the Mechanics and Physics of Solids, 145*, 104147. doi:10.1016/j.jmps.2020.104147.
- Concha, F., Sarabia-Vallejos, M., & Hurtado, D. E. (2018). Micromechanical model of lung parenchyma hyperelasticity. *Journal of the Mechanics and Physics of Solids, 112*, 126–144. doi:10.1016/j.jmps.2017.11.021.
- Coussy, O. (2004). *Poromechanics*. Chichester, England: John Wiley & Sons.

- De Boer, R. (2000). *Theory of Porous Media: Highlights in Historical Development and Current State*. Springer.
- De Souza Neto, E., & Feijóo, R. (2006). Variational foundations of multi-scale constitutive models of solid: Small and large strain kinematical formulation. *LNCC Research & Development Report*, 16. doi:10.1002/9783527632312.ch9.
- Dickinson, A. S., Taylor, A. C., Ozturk, H., & Browne, M. (2011). Experimental validation of a finite element model of the proximal femur using digital image correlation and a composite bone model. *Journal of Biomechanical Engineering*, 133. doi:10.1115/1.4003129.
- Dormieux, L., Molinari, A., & Kondo, D. (2002). Micromechanical approach to the behavior of poroelastic materials. *Journal of the Mechanics and Physics of Solids*, 50, 2203–2231. doi:10.1016/S0022-5096(02)00008-X.
- Ehlers, W., & Bluhm, J. (Eds.) (2002). *Porous Media: Theory, Experiments and Numerical Applications*. Springer-Verlag Berlin Heidelberg.
- Fen-Chong, T., Hervé, E., & Zaoui, A. (1999). Micromechanical modelling of intracellular pressure-induced viscoelastic shrinkage of foams: Application to expanded polystyrene. *European Journal of Mechanics - A/Solids*, 18, 201–218. doi:10.1016/S0997-7538(99)80012-6.
- Fish, J. (2013). *Practical multiscaleing*. John Wiley & Sons. doi:10.1007/978-94-009-3489-4.
- Fung, Y. C. (1988). A model of the lung structure and its validation. *Journal of Applied Physiology*, 64, 2132–2141. doi:10.1152/jappl.1988.64.5.2132.
- Geuzaine, C., & Remacle, J. F. (2009). Gmsh: A 3-D finite element mesh generator with built-in pre- and post-processing facilities. *International Journal for Numerical Methods in Engineering*, 79, 1309–1331. doi:10.1002/nme.2579.
- Guo, L., Vardakis, J. C., Chou, D., & Ventikos, Y. (2020). A multiple-network poroelastic model for biological systems and application to subject-specific modelling of cerebral fluid transport. *International Journal of Engineering Science*, 147, 103204.
- Hambli, R. (2013). Micro-CT finite element model and experimental validation of trabecular bone damage and fracture. *Bone*, 56, 363–374. doi:10.1016/j.bone.2013.06.028.
- Hashin, Z. (1983). Analysis of composite materials—a survey. *Journal of Applied Mechanics*, 50, 481–505. doi:10.1115/1.3167081.
- Hill, R. (1963). Elastic properties of reinforced solids: Some theoretical principles. *Journal of the Mechanics and Physics of Solids*, 11, 357–372. doi:10.1016/0022-5096(63)90036-X.
- Hollister, S. J., & Kikuchi, N. (1992). A comparison of homogenization and standard mechanics analyses for periodic porous composites. *Computational Mechanics*, 10, 73–95. doi:10.1007/BF00369853.
- Hurtado, D. E., Erranz, B., Lillo, F., Sarabia-Vallejos, M., Iturrieta, P., Morales, F., Blaha, K., Medina, T., Diaz, F., & Cruces, P. (2020). Progression of regional lung strain and heterogeneity in lung injury: assessing the evolution under spontaneous breathing and mechanical ventilation. *Annals of Intensive Care*, 10, 107.
- Idiart, M. I., & Lopez-Pamies, O. (2012). On the overall response of elastomeric solids with pressurized cavities. *Comptes Rendus - Mécanique*, 340, 359–368. doi:10.1016/j.crme.2012.02.018.
- Javili, A., Saeb, S., & Steinmann, P. (2017). Aspects of implementing constant traction boundary conditions in computational homogenization via semi-Dirichlet boundary conditions. *Computational Mechanics*, 59, 21–35.
- Johnson, G. R., & Cook, W. H. (1985). Fracture characteristics of three metals subjected to various strains, strain rates, temperatures and pressures. *Engineering Fracture Mechanics*, 21, 31–48. doi:10.1016/0013-7944(85)90052-9.
- Ju, F., Xia, Z., & Sasaki, K. (2008). On the finite element modelling of balloon-expandable stents. *Journal of the Mechanical Behavior of Biomedical Materials*, 1, 86–95. doi:10.1016/j.jmbbm.2007.07.002.
- Julien, J., Garajeu, M., & Michel, J. C. (2011). A semi-analytical model for the behavior of saturated viscoplastic materials containing two populations of voids of different sizes. *International Journal of Solids and Structures*, 48, 1485–1498. doi:10.1016/j.ijsolstr.2011.01.031.
- Kanit, T., Forest, S., Galliet, I., Mounoury, V., & Jeulin, D. (2003). Determination of the size of the

- representative volume element for random composites: Statistical and numerical approach. *International Journal of Solids and Structures*, *40*, 3647–3679. doi:10.1016/S0020-7683(03)00143-4.
- Kantzos, C. A., Cunningham, R. W., Tari, V., & Rollett, A. D. (2018). Characterization of metal additive manufacturing surfaces using synchrotron X-ray CT and micromechanical modeling. *Computational Mechanics*, *61*, 575–580. doi:10.1007/s00466-017-1531-z.
- Koshiyama, K., Nishimoto, K., Ii, S., Sera, T., & Wada, S. (2019). Heterogeneous structure and surface tension effects on mechanical response in pulmonary acinus: A finite element analysis. *Clinical Biomechanics*, *66*, 32–39. doi:10.1016/j.clinbiomech.2018.01.001.
- Koshiyama, K., & Wada, S. (2015). Mathematical model of a heterogeneous pulmonary acinus structure. *Computers in Biology and Medicine*, *62*, 25–32. doi:10.1016/j.combiomed.2015.03.032.
- Larsson, F., Runesson, K., Saroukhani, S., & Vafadari, R. (2011). Computational homogenization based on a weak format of micro-periodicity for RVE-problems. *Computer Methods in Applied Mechanics and Engineering*, *200*, 11–26. doi:10.1016/j.cma.2010.06.023.
- Logg, A., Mardal, K. A., & Wells, G. N. (Eds.) (2012). *Automated Solution of Differential Equations by the Finite Element Method*. Springer. doi:10.1007/978-3-642-23099-8_1.
- Ma, L., Rolfe, B. F., Yang, Q., & Yang, C. (2011). The configuration evolution and macroscopic elasticity of fluid-filled closed cell composites: Micromechanics and multiscale homogenization modelling. *CMES - Computer Modeling in Engineering and Sciences*, *79*, 131–158.
- Mauri, T., Cambiaghi, B., Spinelli, E., Langer, T., & Grasselli, G. (2017). Spontaneous breathing: A double-edged sword to handle with care. *Annals of Translational Medicine*, *5*. doi:10.21037/atm.2017.06.55.
- Nguyen, V. D., Béchet, E., Geuzaine, C., & Noels, L. (2012). Imposing periodic boundary condition on arbitrary meshes by polynomial interpolation. *Computational Materials Science*, *55*, 390–406. doi:10.1016/j.commatsci.2011.10.017.
- Pahr, D. H., & Zysset, P. K. (2008). Influence of boundary conditions on computed apparent elastic properties of cancellous bone. *Biomechanics and Modeling in Mechanobiology*, *7*, 463–476. doi:10.1007/s10237-007-0109-7.
- Patte, C., Genet, M., & Chapelle, D. (2020). A poromechanical model of the lungs. *Submitted*, .
- Patte, C., Genet, M., Fetita, C., Brillet, P.-Y., & Chapelle, D. (2019). Mécanique pulmonaire personnalisée : modélisation et estimation - Application à la fibrose pulmonaire. *CSMA 2019 - 14ème Colloque National en Calcul des Structures*, . URL: <https://hal.archives-ouvertes.fr/hal-02068920>.
- Perić, D., De Souza Neto, E. A., Feijóo, R. A., Partovi, M., & Molina, A. J. (2011). On micro-to-macro transitions for multi-scale analysis of non-linear heterogeneous materials: Unified variational basis and finite element implementation. *International Journal for Numerical Methods in Engineering*, *87*, 149–170. doi:10.1002/nme.3014.
- Perlman, C. E., & Wu, Y. (2014). In situ determination of alveolar septal strain, stress and effective Young’s modulus: An experimental/computational approach. *American Journal of Physiology - Lung Cellular and Molecular Physiology*, *307*, L302–L310. doi:10.1152/ajplung.00106.2014.
- Rausch, S. M., Habertür, D., Stampanoni, M., Schittny, J. C., & Wall, W. A. (2011). Local strain distribution in real three-dimensional alveolar geometries. *Annals of Biomedical Engineering*, *39*, 2835–2843. doi:10.1007/s10439-011-0328-z.
- Roth, C. J., Yoshihara, L., & Wall, W. A. (2017). A simplified parametrised model for lung microstructures capable of mimicking realistic geometrical and mechanical properties. *Computers in Biology and Medicine*, *89*, 104–114. doi:10.1016/j.combiomed.2017.07.017.
- Saeb, S., Steinmann, P., & Javili, A. (2016). Aspects of Computational Homogenization at Finite Deformations: A Unifying Review From Reuss’ to Voigt’s Bound. *Applied Mechanics Reviews*, *68*. doi:10.1115/1.4034024.
- Sarabia-Vallejos, M. A., Zuñiga, M., & Hurtado, D. E. (2019). The role of three-dimensionality and alveolar pressure in the distribution and amplification of alveolar stresses. *Scientific Reports*, *9*, 1–11. URL: <http://www.nature.com/articles/s41598-019-45343-4>. doi:10.1038/s41598-019-45343-4.
- Shakoor, M., Buljac, A., Neggers, J., Hild, F., Morgeneyer, T. F., Helfen, L., Bernacki, M., & Bouchard, P. O. (2017). On the choice of boundary conditions for micromechanical simulations based on 3D imaging.

- International Journal of Solids and Structures*, 112, 83–96. doi:10.1016/j.ijsolstr.2017.02.018.
- Suquet, P. M. (1987). Elements of homogenization for inelastic solid mechanics. In E. Sanchez-Palencia, & A. Zaoui (Eds.), *Homogenization Techniques for Composite Media* (pp. 193–278). Springer-Verlag, Berlin volume 272. doi:10.1038/72256.
- Tawhai, M. H., & Lin, C. L. (2010). Image-based modeling of lung structure and function. *Journal of Magnetic Resonance Imaging*, 32, 1421–1431. doi:10.1002/jmri.22382.
- Terada, K., Hori, M., Kyoya, T., & Kikuchi, N. (2000). Simulation of the multi-scale convergence in computational homogenization approaches. *International Journal of Solids and Structures*, 37, 2285–2311. doi:10.1016/S0020-7683(98)00341-2.
- Vincent, P. G., Monerie, Y., & Suquet, P. (2009). Porous materials with two populations of voids under internal pressure: I. Instantaneous constitutive relations. *International Journal of Solids and Structures*, 46, 480–506. doi:10.1016/j.ijsolstr.2008.09.003.
- Virtanen, P., Gommers, R., Oliphant, T. E., Haberland, M., Reddy, T., Cournapeau, D., Burovski, E., Peterson, P., Weckesser, W., Bright, J., van der Walt, S. J., Brett, M., Wilson, J., Millman, K. J., Mayorov, N., Nelson, A. R., Jones, E., Kern, R., Larson, E., Carey, C. J., Polat, I., Feng, Y., Moore, E. W., VanderPlas, J., Laxalde, D., Perktold, J., Cimrman, R., Henriksen, I., Quintero, E. A., Harris, C. R., Archibald, A. M., Ribeiro, A. H., Pedregosa, F., van Mulbregt, P., Vijaykumar, A., Bardelli, A. P., Rothberg, A., Hilboll, A., Kloeckner, A., Scopatz, A., Lee, A., Rokem, A., Woods, C. N., Fulton, C., Masson, C., Häggström, C., Fitzgerald, C., Nicholson, D. A., Hagen, D. R., Pasechnik, D. V., Olivetti, E., Martin, E., Wieser, E., Silva, F., Lenders, F., Wilhelm, F., Young, G., Price, G. A., Ingold, G. L., Allen, G. E., Lee, G. R., Audren, H., Probst, I., Dietrich, J. P., Silterra, J., Webber, J. T., Slavič, J., Nothman, J., Buchner, J., Kulick, J., Schönberger, J. L., de Miranda Cardoso, J. V., Reimer, J., Harrington, J., Rodríguez, J. L. C., Nunez-Iglesias, J., Kuczynski, J., Tritz, K., Thoma, M., Newville, M., Kümmerer, M., Bolingbroke, M., Tartre, M., Pak, M., Smith, N. J., Nowaczyk, N., Shebanov, N., Pavlyk, O., Brodtkorb, P. A., Lee, P., McGibbon, R. T., Feldbauer, R., Lewis, S., Tygier, S., Sievert, S., Vigna, S., Peterson, S., More, S., Pudlik, T. et al. (2020). SciPy 1.0: fundamental algorithms for scientific computing in Python. *Nature Methods*, 17, 261–272. doi:10.1038/s41592-019-0686-2. arXiv:1907.10121.
- Warren, W. E., & Kraynik, A. M. (1997). Linear elastic behavior of a low-density Kelvin foam with open cells. *Journal of Applied Mechanics*, 64, 787–794. doi:10.1115/1.2788983. arXiv:arXiv:1011.1669v3.
- West, J. (2012). *Respiratory physiology: the essentials*. (9th ed.). Lippincott Williams & Wilkins.
- Youssef, S., Maire, E., & Gaertner, R. (2005). Finite element modelling of the actual structure of cellular materials determined by X-ray tomography. *Acta Materialia*, 53, 719–730. doi:10.1016/j.actamat.2004.10.024.